Chinese Chemical Letters 37 (2026) 112945

Contents lists available at ScienceDirect

Chinese Chemical Letters

journal homepage: www.elsevier.com/locate/cclet

Sodium alginate-modified NiFe layered double hydroxide for robust alkaline seawater oxidation at high current densities

Haipeng Wang[a,b,c,1], Dongrui Li[d,1], Mingyu Liu[d], Yufei Kong[d], Chaoxin Yang[d], Zixiao Li[d], Shengjun Sun[d], Shaochen Wang[a,b,c], Mohamed S. Hamdy[e], Asmaa Farouk[e], Zhengwei Cai[f,*], Xuping Sun[d,g,*]

[a] College of Nuclear Equipment and Nuclear Engineering, Yantai University, Yantai 264005, China
[b] Shandong Key Laboratory of Coastal Zone Environmental Processes and Ecological Security, Yantai University, Yantai 264005, China
[c] Yantai Key Laboratory of Advanced Nuclear Energy Materials and Irradiation Technology, Yantai University, Yantai 264005, China
[d] College of Chemistry, Chemical Engineering and Materials Science, Shandong Normal University, Ji'nan 250014, China
[e] Central Labs & Research Center for Advanced Materials Science (RCAMS), King Khalid University, Abha 61413, Saudi Arabia
[f] Laoshan Laboratory, Qingdao 266237, China
[g] Center for High Altitude Medicine, West China Hospital, Sichuan University, Chengdu 610041, China

ARTICLE INFO

Article history:
Received 30 December 2025
Revised 12 May 2026
Accepted 13 May 2026
Available online 14 May 2026

Keywords:
Sodium alginate
NiFe layered double hydroxide
Seawater oxidation electrocatalysis
Cl^- repulsion
Long-term durability

ABSTRACT

Seawater electrolysis, utilizing coastal resources, holds great promise as a sustainable method for hydrogen production. However, the efficiency of seawater electrolysis is limited by anode catalysts with high overpotentials (η) and short lifespans, due to chloride-induced side reactions. In this study, we introduce sodium alginate (SA) modified NiFe layered double hydroxide nanosheets on Ni foam (SA@NiFe LDH/NF) as a highly efficient and stable electrocatalyst for long-term alkaline seawater oxidation. Our SA@NiFe LDH/NF needs a low η of 362 mV to reach 1000 mA/cm^2, outperforming the unmodified NiFe LDH/NF (425 mV). Furthermore, it maintains continuous electrolysis for 1600 h at current densities of 500 and 1000 mA/cm^2. *In situ* Raman spectroscopy reveals that the SA protective layer not only facilitates NiOOH formation but also establishes a dense electrostatic network *via* carboxyl groups, which repels chloride ions and ensures stable seawater oxidation. This work presents a promising strategy for developing durable, high-performance anodes and highlights the potential of natural polysaccharide coatings for enhancing anode corrosion resistance during the seawater electrolysis process.

© 2026 Published by Elsevier B.V. on behalf of Chinese Chemical Society and Institute of Materia Medica, Chinese Academy of Medical Sciences.

Hydrogen (H_2), with its high calorific value and clean emissions, is widely recognized as a promising green energy source to replace traditional fossil fuels [1–4]. Additionally, it has been shown to serve as a potent therapeutic antioxidant, selectively neutralizing pathogenic oxygen free radicals in the body. This process plays a crucial role in maintaining normal physiological functions and intervening in disease progression [5–7]. Traditional electrolysis methods enable the large-scale production of high-purity green H_2 [8]; however, the development of this technological pathway faces the practical constraint of freshwater scarcity [9–12]. Freshwater resources are scarce, accounting for only 2.5 % of the global water supply. In contrast, seawater is abundant, making up approximately 97.5 % of the world's water resources. Therefore, seawater electrolysis has emerged as a promising strategy to alleviate the freshwater shortage issue [13–28]. The initiation of the chloride evolution reaction (CER) during the seawater electrolysis process, due to high chloride ions (Cl^-) concentrations, leads to reduced oxygen evolution reaction (OER) efficiency and accelerated electrode corrosion. In the alkaline design for seawater electrolysis, the thermodynamic standard potential of the OER is about 480 mV lower than that of the CER [15]. This thermodynamic advantage thus effectively suppresses CER-induced electrode corrosion. However, it remains challenging to drive alkaline seawater oxidation (ASO) under industrial-level current densities (j, >500 mA/cm^2). Therefore, substantial room exists for optimizing OER catalysts to achieve high activity and stability during the ASO process.

Among the various strategies for improving the chlorine corrosion resistance of anodes, the construction of anion-derived passivation layers has emerged as a highly promising approach in recent years [29–32]. The anti-corrosion mechanism originates from the electrostatic repulsion between the anions in the passivation layer

* Corresponding authors.
E-mail addresses: caizhengwei2021@163.com (Z. Cai), xpsun@uestc.edu.cn (X. Sun).
[1] These authors contributed equally to this work.

https://doi.org/10.1016/j.cclet.2026.112945
1001-8417/© 2026 Published by Elsevier B.V. on behalf of Chinese Chemical Society and Institute of Materia Medica, Chinese Academy of Medical Sciences.

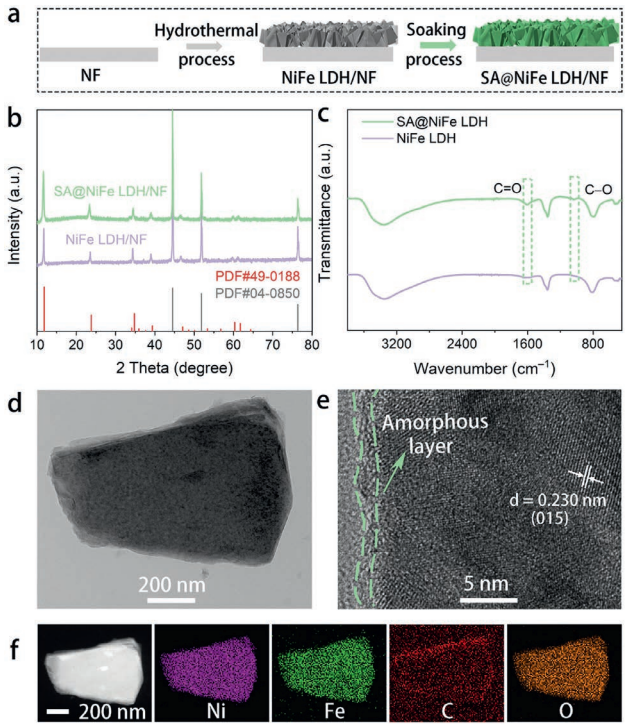


Fig. 1. (a) Schematic fabrication procedure of SA@NiFe LDH/NF. (b) XRD patterns of SA@NiFe LDH/NF and NiFe LDH/NF. (c) FT-IR spectra of SA@NiFe LDH and NiFe LDH. (d) TEM and (e) HRTEM images of SA@NiFe LDH. (f) TEM image and corresponding EDX mappings of SA@NiFe LDH.

and Cl^- in seawater, effectively preventing Cl^- from directly reaching the active sites of the anode catalyst. Numerous studies have explored the use of various inorganic anions for catalyst modification through intercalation or surface adsorption [33,34]. Recent research has also shown that organic anions, such as citrate [35], oxalate [36], benzoate [37], and phytate [18], can serve as effective modifiers for anode catalysts. Sodium alginate (SA) is an abundant organic anion-containing biomacromolecule, making it a promising material for various industrial applications, including pharmaceuticals, food, and cosmetics [38–40]. Due to its hydrophilic nature, with each pyranose ring containing hydroxyl (OH^-) and carboxyl (COO^-) groups, SA readily interacts with metal surfaces [41]. This enables SA to chelate strongly to the surface of anode catalysts. Additionally, the COO^- in SA can form an anionic protective layer on the anode, effectively suppressing chloride-induced corrosion and promoting efficient and stable ASO. Compared with other reported SA-modified catalysts, SA@NiFe LDH/NF features a simpler synthesis procedure, lower energy consumption, and superior electrochemical performance [42].

In this study, SA-modified NiFe layered double hydroxide on Ni foam (SA@NiFe LDH/NF) was successfully synthesized through a facile hydrothermal and immersion route as an efficient and stable ASO electrocatalyst. With the introduction of SA, the catalytic activity of NiFe LDH/NF was significantly enhanced, requiring a low overpotential (η) of 362 mV to achieve an industrial-level j of 1000 mA/cm^2. Furthermore, the COO^- in SA can effectively repel Cl^- and protect the active sites from chloride corrosion. Benefiting from this protection, SA@NiFe LDH/NF demonstrates exceptional durability in alkaline seawater, retaining stable operation over 600 h at 500 mA/cm^2 and 1000 h at 1000 mA/cm^2.

Fig. 1a illustrates the preparation process of SA@NiFe LDH/NF. Fig. 1b reveals X-ray diffraction patterns (XRD) of SA@NiFe LDH/NF and NiFe LDH/NF, which clearly display the characteristic diffraction peaks corresponding to NiFe LDH (PDF #49–0188) and NF (PDF #04–0850). No shift was observed in the diffraction peaks, revealing that the crystal structure of NiFe LDH/NF keeps constant. Characteristic vibrational bands at 1034 and 1608 cm^{-1} are observed in the Fourier transform infrared spectroscopy (FT-IR) spectra of both catalysts (Fig. 1c), respectively, stemming from the stretching vibrations of C–O and C=O bonds [42]. Vibrational features associated with SA@NiFe LDH is more pronounced, owing to the introduction of SA. As observed from the scanning electron microscopy (SEM) images (Figs. S1 and S2 in Supporting information), both catalysts are firmly grown on the NF surface, and exhibit a nanosheet morphology. Transmission electron microscopy (TEM) image (Fig. 1d) confirms that SA@NiFe LDH exhibits a sheet morphology. Moreover, high-resolution TEM (HRTEM) image (Fig. 1e) shows a distinct lattice spacing of 0.230 nm, assigned to the (015) crystal plane of NiFe LDH. And identify an amorphous layer on the surface of NiFe LDH. TEM image and corresponding energy-dispersive X-ray spectroscopy (EDX) mappings (Fig. 1f) further validates that the nanosheet surface exhibits a uniform distribution of Ni, Fe, C, and O elements. Compared with the NF, SA@NiFe LDH/NF exhibits excellent superhydrophilicity, and the liquid droplets spread rapidly upon contacting the material surface (Fig. S3 in Supporting information). This property allows SA@NiFe LDH/NF to exhibit excellent interfacial compatibility with electrolytes.

X-ray photoelectron spectroscopy (XPS) measurements offered supplementary details pertaining to the catalyst's surface chemical composition and valence states. The Ni 2p spectra (Fig. S4a in Supporting information) exhibit characteristic peaks for Ni^{2+} (855.75 and 873.68 eV), and Ni^{3+} (857.47 and 876.47 eV) [32,36], along with satellite (Sat.) peaks at 862.71 and 879.88 eV. The Fe 2p spectra (Fig. S4b in Supporting information) exhibit peaks for Fe^{2+} (706.4 and 719.04 eV), Fe^{3+} (712.41 and 724.81 eV), and Sat. peaks (715.76 and 727.13 eV) [43]. The C 1s spectrum (Fig. S4c in Supporting information) shows characteristic peaks of C=C (284.84 eV), C–O–C (285.78 eV), and O–C=O (289.26 eV), respectively [42]. The O 1s spectrum (Fig. S4d in Supporting information) shows characteristic peaks of M–O (529.61 eV), M–OH (531.35 eV), and adsorbed H_2O (532.08 eV), respectively [44]. Notably, the Ni 2p and Fe 2p peaks in SA@NiFe LDH show a shift in the positive direction relative to NiFe LDH. This phenomenon provides direct evidence that the introduction of SA can modulate the electronic structure of the catalyst. Following the successful synthesis of the catalyst, a three-electrode test system with an alkaline electrolyte (1 mol/L KOH + seawater) was employed to systematically evaluate its OER electrocatalytic performance. Comprehensive details about the seawater used in the experiment are presented in Table S1 (Supporting information). We investigated the effect of SA content on the OER performance. As shown in Fig. S5 (Supporting information), $SA_{1/6}$@NiFe LDH/NF offers the superior OER activity, and thus, the following tests were all performed using this electrode. Linear sweep voltammetry (LSV) curves (Fig. 2a) demonstrate that the catalyst exhibits outstanding electrocatalytic activity in the alkaline seawater system. When the j reaches 1000 mA/cm^2, the required η is only 362 mV, which is considerably lower than those of NiFe LDH/NF (425 mV) and RuO_2/NF (564 mV) (inset of Fig. 2a). The LSV curves without iR compensation are presented in Fig. S6 (Supporting information). Furthermore, it is noteworthy that the electrocatalytic performance of SA@NiFe LDH/NF exceeds that of most comparable catalysts reported thus far (Table S2 in Supporting information). Tafel slopes corresponding to both catalysts in different j ranges are illustrated in Fig. S7 (Supporting information). The data show that the Tafel slope values of the catalyst are the lowest within the different j ranges. Meanwhile, the $\Delta\eta/\Delta\log|j|$ ratio of the catalyst is also at the lowest level. These results indicate that the catalyst exhibits faster reaction kinetics under different j. Cyclic voltammetry (CV) measurements with scan rates ranging

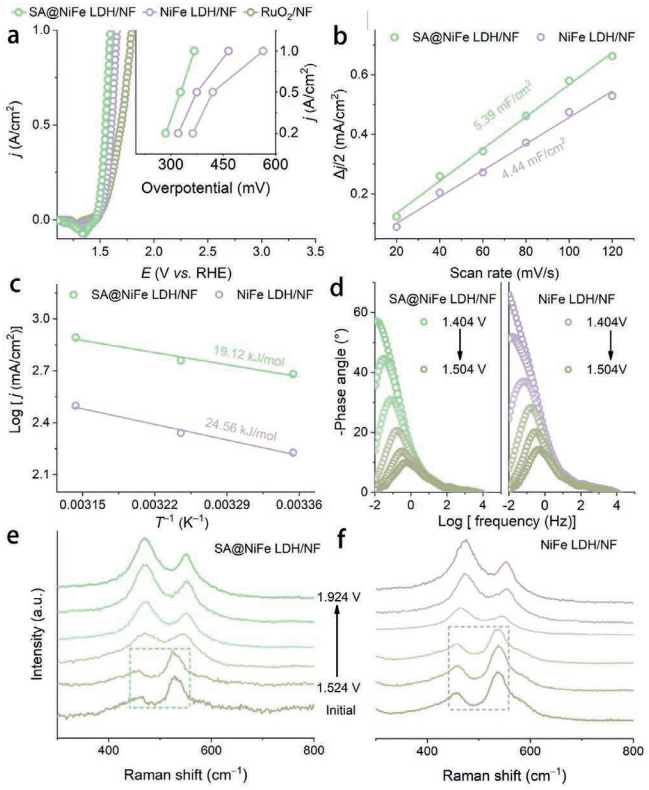


Fig. 2. (a) LSV curves (inset: j at different η) of SA@NiFe LDH/NF, NiFe LDH/NF, and RuO_2/NF. (b) C_{dl} curves, (c) Arrhenius plots, and (d) Bode plots of SA@NiFe LDH/NF and NiFe LDH/NF. *In situ* Raman spectra recorded for (e) SA@NiFe LDH/NF and (f) NiFe LDH/NF during the ASO process.

from 20 mV/s to 120 mV/s were employed to determine the electrochemical double-layer capacitance (C_{dl}). The results reveal that the C_{dl} value of SA@NiFe LDH/NF reached 5.39 mF/cm^2, which was higher than that of NiFe LDH/NF (4.44 mF/cm^2). This result indicates that SA@NiFe LDH/NF possesses a larger electrochemically active surface area (ECSA), corresponding to more exposed and available catalytic active sites on its surface (Fig. 2b). The ECSA-normalized LSV curves show that the intrinsic activity of SA@NiFe LDH/NF is better than that of NiFe LDH/NF (Fig. S8 in Supporting information). The turnover frequency (TOF) was derived from CV measurements conducted at a series of scan rates in Fig. S9 (Supporting information). As depicted in Fig. S10 (Supporting information), SA@NiFe LDH/NF exhibits a higher value in comparison with NiFe LDH/NF, which attests to its superior intrinsic electrocatalytic activity. Fig. S11 (Supporting information) presents the LSV curves under different temperature conditions. Based on the LSV test data obtained at various temperatures, we further calculated the activation energy for the OER (Fig. 2c). The data demonstrate that the activation energy of SA@NiFe LDH/NF (19.12 kJ/mol) is significantly lower than that of NiFe LDH/NF (24.56 kJ/mol). This result demonstrates the outstanding electrocatalytic activity of SA@NiFe LDH/NF. To further elucidate the reaction kinetic mechanism of the OER, electrochemical impedance spectroscopy (EIS) tests were conducted over a potential range of 1.404–1.504 V. The Nyquist plots (Fig. S12 in Supporting information) show that the diameter of the semicircle decreased systematically with increasing applied potential, implying a reduction in charge transfer resistance (R_{ct}) that is directly linked to the enhanced OER activity. The Nyquist plot of SA@NiFe LDH/NF shows a distinct semicircular feature when the applied potential is increased to 1.424 V, reflecting a decrease in the R_{ct}, which indicates that the OER process is initiated after reaching 1.424 V [36]. In contrast, NiFe LDH/NF exhibits no obvious semicircular pattern at this potential, and a higher potential is required to observe this characteristic. Meanwhile, the Bode plots at different potentials (Fig. 2d) indicate that SA@NiFe LDH/NF exhibits a small initial phase angle, and the phase angle changes rapidly within the potential range of 1.404–1.504 V. These results suggest that the defect-rich structure and SA-induced interfacial modulation facilitate charge transport and thereby accelerate the OER kinetics. Collectively, these characterization results confirm that the introduction of SA effectively optimizes the interfacial charge transfer kinetics of the catalyst, providing a kinetic basis for its exceptional OER performance. EIS measurements (Fig. S13 and Table S3 in Supporting information) reveal that SA@NiFe LDH/NF exhibits a R_{ct} of only 3.85 Ω, which is distinctly lower than that of NiFe LDH/NF ($R_{ct} = 6.03$ Ω). Concurrently, SA@NiFe LDH/NF shows a lower ohmic resistance ($R_s = 2.45$ Ω) in comparison with NiFe LDH/NF ($R_s = 2.58$ Ω), which collectively indicate an effective enhancement in the electrical conductivity of SA@NiFe LDH/NF. These characteristics directly verify that SA@NiFe LDH/NF possesses superior charge transfer kinetics and electronic conductivity.

EIS measurements were employed to evaluate the bubble evolution kinetics of both catalysts. Notably, SA@NiFe LDH/NF displays a smoother impedance response fluctuation (Fig. S14 in Supporting information), which is indicative of a more efficient sequence of bubble nucleation, growth, and detachment processes. To gain further insights into the electrocatalytic behavior of the as-prepared material, *in situ* XRD measurements (Fig. S15 in Supporting information) were performed during the OER process at 0, 5, 10, 20, and 30 h. The weakened NiFe LDH diffraction peaks indicate progressive structural reconstruction during OER, likely associated with the generation of active amorphous NiOOH species [45]. Furthermore, *in situ* Raman spectroscopy measurements intuitively visualize the potential-dependent dynamic structural evolution of SA@NiFe LDH/NF during the ASO process. As shown in Figs. 2e and f, the observed Raman peaks exhibit a shift toward higher wavenumbers. This phase is characterized by the $\delta(Ni^{3+}$–O) and $\nu(Ni^{3+}$–O) vibrations [46,47]. Raman analysis further reveals that the interaction between SA and NiFe LDH involves coordination/chelation effects rather than simple physical adsorption. After SA modification, the main Ni^{2+}–OH vibration at 450–465 cm^{-1} exhibits a blue shift of 5–15 cm^{-1} together with significant peak broadening, indicating a reconstructed local coordination environment around Ni species, strengthened metal–oxygen bonding, and reduced structural ordering of the LDH layers. Meanwhile, the defect-associated Ni^{2+}–O band at 525–535 cm^{-1} shows an obvious blue shift and enhanced intensity, with the intensity ratio I_{530}/I_{460} increasing to 1.06, suggesting that SA-induced chelation generates abundant lattice defects and local disorder in the LDH framework [48]. These results indicate that SA can coordinate with surface-exposed metal centers and thereby modulate both the local electronic/coordination structure and the interfacial charge distribution. Such coordination-assisted interfacial coupling, together with the negatively charged SA layer, contributes to the formation of a dense electrostatic network that suppresses Cl^- approach to the catalyst surface. Notably, in comparison with the reference sample, the catalyst displays an earlier peak shift at a lower voltage, showing that the presence of SA facilitates the formation of γ-NiOOH [49].

To further elucidate the catalytic behavior during the OER process, density functional theory (DFT) calculations were performed. The results show that the potential-determining step (PDS) for OER on Fe-site NiFe LDH is the formation of *OOH (Fig. S17 in Supporting information), with a corresponding free-energy increase of 2.60 eV. In comparison, the SA(Fe-site)-NiFe LDH system also identifies the *OOH formation step as the PDS, but with a markedly reduced free-energy barrier of 1.89 eV. These results indicate that SA modulation effectively lowers the energy barrier of the key OER

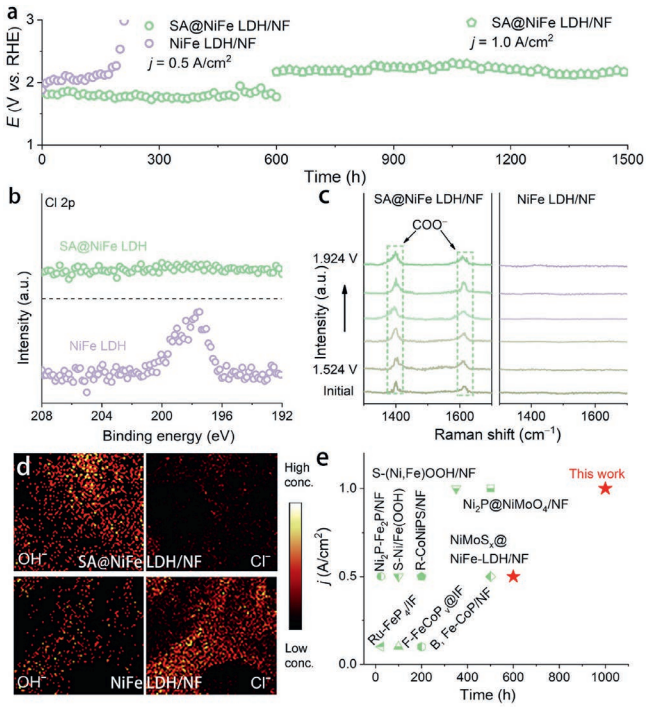


Fig. 3. (a) Chronopotentiometry curves of SA@NiFe LDH/NF and NiFe LDH/NF. (b) XPS spectra in Cl 2p regions of SA@NiFe LDH and NiFe LDH after the stability test. (c) *In situ* Raman spectra for SA@NiFe LDH/NF and NiFe LDH/NF. (d) TOF-SIMS mapping of OH^- and Cl^- fragments on the two types of electrode surfaces following a 12 h test. (e) Comparison of catalysts lifetime in 1 mol/L KOH + seawater.

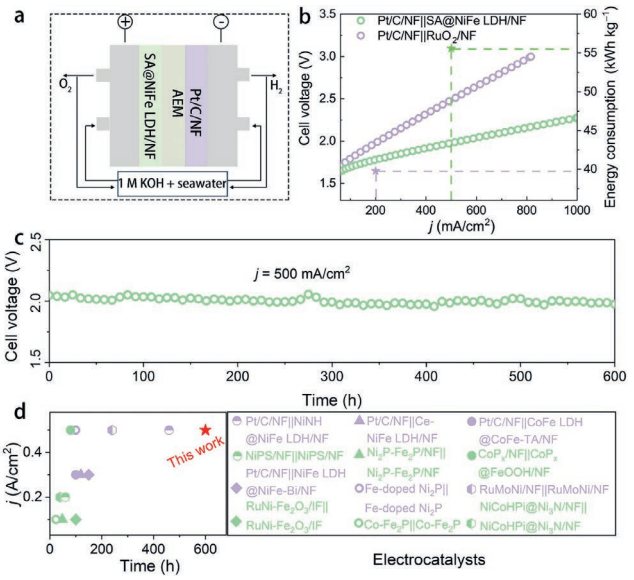


Fig. 4. (a) Schematic diagram of AEM-based electrolyzer. (b) Polarization curves of Pt/C/NF||SA@NiFe LDH/NF and Pt/C/NF||RuO_2/NF, and H_2 production cost of Pt/C/NF||SA@NiFe LDH/NF. (c) Stability measurement. (d) Comparison of electrolyzer performance in different reaction conditions.

intermediate, thereby promoting the reaction kinetics and enhancing the catalytic activity.

The electrochemical durability was evaluated at high *j* of 500 and 1000 mA/cm^2. SA@NiFe LDH/NF demonstrates significantly enhanced stability, operating for 600 h and 1000 h, respectively. After 1600-h of operation, it can still run stably for another 400 h at a high *j* of 2 A/cm^2, demonstrating outstanding long–term stability (Fig. S18 in Supporting information). In sharp contrast, NiFe LDH/NF electrode is stable for merely 220 h at 500 mA/cm^2 (Fig. 3a). Fig. 3b intuitively demonstrates the excellent Cl^- blocking capability of SA@NiFe LDH, which is evidenced by the complete absence of the characteristic Cl 2p signal in its spectrum. In contrast, the spectrum of NiFe LDH shows the appearance of distinct peaks attributable to chlorine species. The residual active chlorine in the post-electrolysis electrolyte was quantified *via* the *N,N*–diethyl-*p*-phenylenediamine colorimetric method [50]. Ultraviolet-visible spectroscopic data (Figs. S19 and S20 in Supporting information) show that after long-term stability testing, the active chlorine content in SA@NiFe LDH/NF electrolyte is significantly reduced compared to that in NiFe LDH/NF electrolyte, providing strong experimental evidence to support the previous conclusions. As shown in Fig. S21 (Supporting information), at a *j* of 1000 mA/cm^2, the actual collected oxygen volume closely matches the theoretical value, indicating that faradaic efficiency (FE) for ASO is nearly 100 %. The low active chlorine content and high FE confirm that the catalyst has higher OER selectivity than CER under high *j* conditions. Fig. S22 (Supporting information) shows that the catalyst has a positive corrosion potential and low corrosion *j*. To further investigate the underlying reasons for its exceptional ASO stability, we conducted *in situ* Raman spectroscopy (Fig. 3c). Peaks corresponding to COO^- groups are observed at 1413 and 1625 cm^{-1} in the spectra of SA@NiFe LDH/NF [51,52], features not found in NiFe LDH/NF. Remarkably, the COO^- group remains stable even as the voltage increases enables a stable electrostatic layer on the catalyst surface. This electrostatic layer effectively repels Cl^-, contributing to the stable ASO performance. As presented in Fig. 3d, time-of-flight secondary ion mass spectrometry (TOF-SIMS) analysis reveals that SA@NiFe LDH/NF surfaces have distinctly higher OH^- coverage and significantly lower Cl^- signals than NiFe LDH/NF. Compared with most reported ASO catalysts (Fig. 3e and Table S4 in Supporting information), the catalyst demonstrates superior stability performance. Notably, systematic characterizations, including morphology, crystal phase, and chemical composition, were carried out after the stability test to evaluate the structural stability of the catalyst. The results demonstrate that the morphology and overall crystal phase of SA@NiFe LDH/NF are well preserved without obvious changes, further verifying its excellent long-term stability (Figs. S23–S25 in Supporting information). In addition, the Ni 2p and Fe 2p XPS spectra show that the Ni and Fe species remain in highly oxidized states after the stability test, suggesting the formation of catalytically active oxyhydroxide species during the ASO process. These results indicate that SA@NiFe LDH/NF can maintain structural integrity while undergoing surface reconstruction into the active NiOOH-like phase under operating conditions.

To assess practical applicability, an anion exchange membrane (AEM) electrolyzer (Pt/C/NF||SA@NiFe LDH/NF) was assembled (Fig. 4a). As illustrated in Fig. 4b, the AEM-based electrolyzer exhibits corresponding cell voltages of 1.78 and 1.97 V at *j* of 200 and 500 mA/cm^2 respectively, which are significantly lower than those of the Pt/C/NF||RuO_2/NF. Moreover, the system operates with lower energy consumption, requiring only 39.79 and 55.57 kWh/kg H_2 at 200 and 500 mA/cm^2, demonstrating higher energy efficiency. To evaluate the scalability of the synthesis strategy and its potential for practical application, large-area SA@NiFe LDH/NF electrodes (2×2 cm^2) were successfully prepared and further assembled into corresponding electrolyzers. The resulting device maintained stable operation for over 80 h, indicating that the present synthesis method can be readily extended from small laboratory electrodes to larger electrode areas while preserving reliable performance. These results demonstrate the promising scalability of our approach and highlight the practical potential of SA@NiFe LDH/NF for large-scale H_2 production. Importantly, the system exhibits supe-

rior durability compared to other self-supporting catalysts, achieving stable operation for 600 h at 500 mA/cm^2 (Figs. 4c, d, and Table S4). This fully demonstrates its excellent operational stability under seawater electrolysis conditions.

In summary, SA@NiFe LDH/NF catalyst was successfully fabricated *via* the impregnation method in this work. The SA@NiFe LDH/NF can effectively suppress the chloride-mediated corrosion, thus enabling long-term stable seawater electrolysis. Demonstrating remarkable stability, the catalyst maintains continuous operation for 1000 h in ASO while achieving a low η of only 362 mV at 1000 mA/cm^2. Notably, the coordination interactions between SA and NiFe LDH/NF not only enhance OER activity but also enable efficient Cl^- repulsion through electrostatic effects, thereby improving the catalytic stability during the ASO process. Furthermore, when the catalyst was assembled into the Pt/C/NF||SA@NiFe LDH/NF electrode couple and applied in an AEM, it achieved stable operation for 600 h at 500 mA/cm^2, demonstrating strong potential for practical use. This work not only introduces a high-performance and durable catalyst from earth-abundant materials for ASO but also opens a promising avenue for designing chloride-resistant catalysts.

CRediT authorship contribution statement

Haipeng Wang: Writing – original draft, Data curation. **Dongrui Li:** Writing – original draft, Data curation. **Mingyu Liu:** Data curation. **Yufei Kong:** Formal analysis. **Chaoxin Yang:** Formal analysis. **Zixiao Li:** Investigation. **Shengjun Sun:** Investigation. **Shaochen Wang:** Resources. **Mohamed S. Hamdy:** Validation. **Asmaa Farouk:** Validation. **Zhengwei Cai:** Writing – review & editing. **Xuping Sun:** Writing – review & editing, Conceptualization.

Declaration of competing interest

The authors declare that they have no known competing financial interests or personal relationships that could have appeared to influence the work reported in this paper.

Acknowledgment

M. S. Hamdy and A. Farouk extend their appreciation to the Deanship of Research and Graduate Studies at King Khalid University for funding this work through Large Research Project under Grant No. RGP2/29/46.

Supplementary materials

Supplementary material associated with this article can be found, in the online version, at doi:10.1016/j.cclet.2026.112945.

References

[1] A. Goldthau, Nature 546 (2017) 203–205.
[2] M. Goel, G. Sen, Climate Action and Hydrogen Economy: Technologies Shaping the Energy Transition, Springer Nature, Singapore, 2024.
[3] H. Jin, H. Yu, H. Li, et al., Angew. Chem. Int. Ed. 61 (2022) e202203850.
[4] H. Valera, A.K. Agarwal, Hydrogen As Emerging Fuel For De-Fossilizing Transport Sector, Springer, Singapore, 2024.
[5] I. Ohsawa, M. Ishikawa, K. Takahashi, et al., Nat. Med. 13 (2007) 688–694.
[6] J. Slezák, B. Kura, Molecular Hydrogen in Health and Disease, Springer, Switzerland, 2024.
[7] Z. Jiang, M. Ainiwaer, J. Liu, et al., Biomater. Sci. 12 (2024) 4136–4154.
[8] J. Ge, X. Wang, H. Tian, et al., Chin. Chem. Lett. 36 (2025) 109906.
[9] J. Wang, W. Cui, Q. Liu, et al., Adv. Mater. 28 (2016) 215–230.
[10] I. Roger, M.A. Shipman, M.D. Symes, Nat. Rev. Chem. 1 (2017) 0003.
[11] P. Greve, T. Kahil, J. Mochizuki, et al., Nat. Sustain. 1 (2018) 486–494.
[12] S.L. Postel, Ecol. Appl. 10 (2000) 941–948.
[13] M. Yang, J. Ding, Z. Wang, et al., Chin. Chem. Lett. 36 (2025) 110861.
[14] J. Liang, Z. Li, M. Zhang, et al., Adv. Mater. 37 (2025) 2503660.
[15] W. Tong, M. Forster, F. Dionigi, et al., Nat. Energy 5 (2020) 367–377.
[16] J. Liang, Z. Li, X. He, et al., Mater. Today 69 (2023) 193–235.
[17] C. Yang, K. Dong, L. Zhang, et al., Inorg. Chem. 62 (2023) 7976–7981.
[18] J. Liang, Z. Cai, Z. Li, et al., ACS Nano 19 (2025) 1530–1546.
[19] X. He, Y. Yao, M. Zhang, et al., Nat. Commun. 16 (2025) 5541.
[20] Y. Zhao, B. Jin, Y. Zheng, et al., Adv. Energy Mater. 8 (2018) 1801926.
[21] Z. Wang, C. Wang, L. Ye, et al., Inorg. Chem. 61 (2022) 15256–15265.
[22] G.H. Gao, R.Z. Zhao, Y.J. Wang, et al., Chin. Chem. Lett. 35 (2024) 109181.
[23] K. Jiang, W. Liu, W. Lai, et al., Inorg. Chem. 60 (2021) 17371–17378.
[24] Q. Sha, S. Wang, L. Yan, et al., Nature 639 (2025) 360–367.
[25] W. Zhang, Y. Wei, J. Li, et al., Fuel 377 (2024) 132782.
[26] Z. Li, J. Liang, S. Hong, et al., Nat. Commun. 16 (2025) 10327.
[27] J. Liang, Z. Cai, Z. Li, et al., Nat. Commun. 15 (2024) 2950.
[28] K. Wang, J. Qiu, Z. Wu, et al., Chin. Chem. Lett. 36 (2025) 109993.
[29] X. Sun, W. Shen, H. Liu, et al., Nat. Commun. 15 (2024) 10351.
[30] L. Ye, Z. Chen, X. Xu, et al., Inorg. Chem. 63 (2024) 20859–20869.
[31] Z. Wu, J. Li, J. Ying, et al., Small 21 (2025) 2504302.
[32] L. Yao, J. Yang, Z. Li, et al., Inorg. Chem. 64 (2025) 2458–2467.
[33] Y. Yu, W. Zhou, X. Zhou, et al., Adv. Funct. Mater. 35 (2025) 2419871.
[34] H. Wang, Z. Li, S. Hong, et al., Small 20 (2024) 2311431.
[35] J. Song, Z. Li, S. Sun, et al., J. Colloid. Interf. Sci. 679 (2025) 1–8.
[36] X. Wang, Z. Li, S. Sun, et al., J. Colloid. Interf. Sci. 662 (2024) 596–603.
[37] L. Zhang, J. Liang, L. Yue, et al., Nano Res. Energy 1 (2022) e9120028.
[38] A.E. Mohammed, L.R. Abdalhalim, K.M. Atalla, et al., Rend. Lincei Sci. Fis. Nat. 34 (2023) 415–425.
[39] X. Li, K. Li, J. Wu, et al., Sep. Purif. Technol. 339 (2024) 126637.
[40] N.N. Indriyani, J. Al-Anshori, T. Wahyudi, et al., J. Biomater. Sci., Polym. Ed. 35 (2024) 989–1007.
[41] H. Wang, L. Yang, Y. Yang, et al., Int. J. Biol. Macromol. 292 (2025) 139151.
[42] S. Raza, A.U. Rehman, C. Chen, et al., J. Mater. Chem. A 13 (2025) 4390–4403.
[43] Y. Yao, S. Sun, H. Zhang, et al., J. Energy Chem. 91 (2024) 306–312.
[44] Y. Ren, X. Zhang, C. Yang, et al., Inorg. Chem. 64 (2025) 21185–21193.
[45] S. Kumaravel, R. Jayakumar, K.K. Saravanan, et al., Dalton Trans. 51 (2022) 17454–17465.
[46] W. Jiang, Z. Li, S. Sun, et al., Catal. Sci. Technol. 15 (2025) 4386–4391.
[47] Y. Zhou, J. Gao, M. Ju, et al., ACS Appl. Mater. Interfaces 16 (2024) 28526–28536.
[48] L. Huang, M. Liu, S. Sun, et al., J. Mater. Chem. A 14 (2026) 7382–7387.
[49] T. Li, C. Yang, Z. Cai, et al., Mater. Today Phys. 50 (2025) 101612.
[50] J. Vos, M. Koper, J. Electroanal. Chem. 819 (2018) 260–268.
[51] M.M. Campos Vallette, N.P. Chandía, E. Clavijo, et al., J Raman Spectrosc. 41 (2010) 758–763.
[52] T. Schmid, A. Messmer, B.S. Yeo, et al., Anal. Bioanal. Chem. 391 (2008) 1907–1916.